JOURNAL OF MATERIALS SCIENCE 30 (1995) 2769–2784

Mechanical properties and microstructures of sol–gel derived ceramic-matrix composites

J. M. CHANT, S. M. BLEAY*, B. HARRIS, R. RUSSELL-FLOYD†, R. G. COOKE, V. D. SCOTT
School of Materials Science, University of Bath, Claverton Down, Bath, UK
**Structural Materials Centre, DRA, Farnborough, UK*

A sol–gel process involving rapid freezing ("freeze gelation") permits the fabrication of ceramic-matrix composite components at low sintering temperatures, to near-net shape and with low shrinkage. The effects of matrix composition and sintering temperature on the microstructures, mechanical properties and damage modes of sol–gel-silica/unidirectional carbon-fibre composites obtained by filament winding were explored. Matrix properties were modified by the incorporation of amorphous silica and glass-ceramic particles and amorphous silica and quartz particles into the colloidal silica sol. Flexural testing and scanning electron microscopy of fracture surfaces were used to determine mechanical properties and fracture mechanisms, whilst transmission and scanning electron microscopy, optical microscopy and X-ray diffraction were used to characterize the microstructures. A transition from a tough mode of fracture, involving appreciable fibre pull-out, to a brittle mode was observed when the sintering temperature was increased beyond 900 °C. The brittleness was attributed to the formation of α-cristobalite whose high thermal expansion coefficient caused matrix cracking and fibre clamping. In one matrix system, α-cristobalite was formed in the amorphous silica filler particles, and in the other in the sol–gel matrix itself. A complex pattern of directional porosity, an artefact of the freeze gelation process, was found to influence the crack-growth behaviour during mechanical testing.

1. Introduction

The intrinsic high stiffness, high hardness, chemical inertness and refractoriness of ceramics derive from the strength of their ionic and covalent bonding [1]. Unfortunately, this bonding permits little or no movement of dislocations, even at modest temperatures, and leads ultimately to brittleness. Moreover, the stress levels at which failures occur are a small fraction of those theoretically achievable. Because a distribution of flaw sizes is evident in real materials, so then do ceramics exhibit a distribution of strength values; from a design engineer's perspective, ceramics are unreliable. The objectives that must be met if ceramics are to become viable engineering materials are: to increase toughness, to decrease sensitivity to flaws, to increase reliability (i.e. to increase the consistency of property values) and, finally, to realize the potential strength of ceramics.

Crack-interaction and crack-shielding mechanisms in monolithic ceramics have been invoked through the engineering of their microstructures [2–4]. The addition of second-phase particles, such as whiskers or transformation-toughening particles of zirconia, for example, has produced modest increases in toughness, typically by a factor of 2–3. By far the most impressive increases in toughness, however, are seen when ceramic fibres are incorporated into brittle, ceramic matrices. Some two decades ago the potential of ceramic-matrix composites was demonstrated [5]. The incorporation of carbon fibres into glass and glass-ceramic matrices has led to composite materials having toughnesses some 20 times greater than the monolithic matrix materials and which can withstand large tensile strains prior to final failure, exhibiting a significant degree of damage tolerance.

1.1. Fabrication of ceramic-matrix composites

Fabrication methods applicable to ceramic-matrix composites have been reviewed by several authors [6–9]. Phillips [9] asserts that all of the successful techniques for the manufacture of ceramic-matrix composites involve processing at elevated temperatures, typically above 1000 °C. At such high temperatures, physical and chemical compatibility between the reinforcing fibre/whisker and matrix are important. Differences in the thermal expansion coefficients of the fibres and matrix will give rise to thermally induced residual stresses which will alter the

† Now deceased.

0022–2461

mechanical properties of the composite. The high processing temperatures may also result in degradation of the fibres or in fibre/matrix interfacial reactions which generate high interfacial bond strengths and hence lead to brittle, low-strength composites.

Any successful fabrication process must fulfil several requirements: the fibres must not be damaged in any way and must retain their intended alignments; interface properties should be controllable, as described above; and the matrix should attain sufficient density for its optimum mechanical properties to be realized. Moreover, the method should be applicable to a variety of fibre/matrix combinations, be as cheap and simple as possible and be able to produce complex shapes with minimal post-fabrication machining.

Processing methods which utilize sol–gel technology have been explored as a possible means of achieving these aims [10]. A colloidal system may be defined as comprising a disperse phase with at least one dimension between 1 nm and 1 μm in a dispersion medium, typically aqueous. A colloidal suspension of solid ceramic particles (sol) may, through controlled interruption of the small inter-particle forces which control sol stability, be converted to a non-crystalline gel. Such a gel may then be dried and sintered to form a solid body. Advantages of sol–gel methods over conventional ceramic processing routes include high matrix homogeneity (because the fine ceramic particles are intimately mixed in the colloidal state), the ability to prepare compositions which are difficult to achieve by conventional methods, and relatively low sintering temperatures (as a consequence of the high reactivity which arises from the very high surface area of the gel).

Historically, however, the major drawback to the application of sol–gel processing for the production of monoliths has been the high level of shrinkage which occurs as the gel dries out during evaporation of the original solvent and during subsequent sintering, and extensive residual fine-scale porosity. Non-reactive fillers and reinforcing fibres may reduce the volume shrinkage to levels as low as 7% from typically 25% [7]. Residual stresses in the body are likely to cause local matrix cracking. Expulsion of the solvent also results in porosity in the solid which, because most engineering applications require dense bodies, must be filled by liquid- or gas-phase infiltration.

1.2. Freeze gelation (sol–gel) fabrication method

A sol–gel processing route developed at Bath University [11] shows potential for fulfilling certain of the requirements outlined above and has been used to produce the materials studied in this paper. The freeze gelation process involves rapidly freezing a silica sol to produce a porous, easily handled green body which may then be infiltrated and sintered. The principal advantages of the approach are its low cost, low shrinkage levels (typically less than 1%), low sintering temperatures, applicability to both continuous- and short-fibre systems and its ability to produce a variety of shapes.

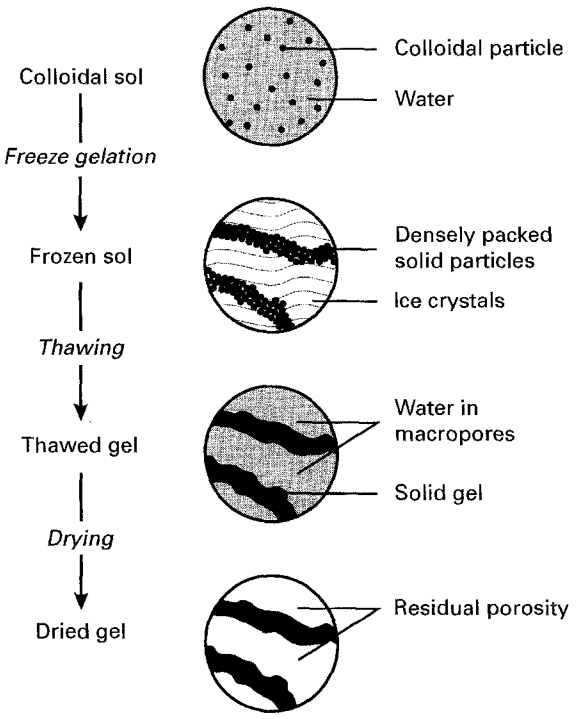

Figure 1 Schematic representation of the sol–gel freeze gelation process.

The process is illustrated schematically in Fig. 1. The silica sol, filler and reinforcement are rapidly frozen to well below 0 °C. The freezing process causes the formation of ice crystals (from the original aqueous solvent), with a consequential small increase in the volume occupied by the water. A gel is formed in the regions between the ice crystals. On warming back to room temperature and drying off the water, the solid may be readily handled and exhibits minimal shrinkage. Residual porosity, in the regions previously occupied by the ice crystals, is large (e.g. 10 μm) and open, presenting the possibility of infiltration (gas or liquid phase) followed by sintering to densify the bodies.

Conventional polymer–matrix composite processing techniques permit the fabrication of a variety of shapes; casting and filament winding have already been used, and a resin transfer moulding approach is feasible. Although the technique is currently restricted to silica sols, an improved understanding of the mechanisms of freeze gelation in silica should permit the extension of the freeze gel process to other ceramic sols of interest (e.g. zirconia).

1.3. Objectives of the work

The roles of the different fabrication variables involved in the freeze gelation process need to be properly evaluated if the potential of the technique is to be realized. In this work, matrix composition and sintering temperature have been controlled in order to assess their effects upon composite microstructures and mechanical properties. Particular attention was paid to the patterns of matrix porosity within the materials, to composite damage behaviour and to the possibility of phase changes during sintering which may lead to residual stresses.

2. Experimental procedure

2.1. Materials studied

Two matrix systems were investigated (Table I). The matrix in composite samples designated "HC" consisted of a colloidal silica sol of average particle size 125 nm with dried, amorphous silica and CMA6 (a proprietary glass) fillers. Series "XQ" samples were prepared with a colloidal silica of average particle size 25 nm, with dried, amorphous silica and quartz fillers. Unidirectional composites using a carbon-fibre reinforcement (Torayca T300) were prepared by a filament-winding technique involving freeze gelation, as shown schematically in Fig. 2. The carbon fibres were passed through a desizing furnace at 700 °C and then through a bath containing a mixture of the colloidal silica and filler particles. The impregnated fibres were then wound on to a hollow, hexagonal mandrel of width 100 mm. Liquid nitrogen was poured into the mandrel to cause freeze gelation of the matrix. Plates were removed from the drum, thawed to room temperature, dried at around 50 °C and finally cut into specimens of nominal dimensions 100 mm × 10 mm. Specimens were 3–5 mm thick. The plates were then infiltrated under pressure with a colloidal silica of particle size ~ 7 nm, sintered at 600 °C in argon and left to cool to ambient temperature in argon. Following seven more infiltrations, the samples were sintered at temperatures of 600 °C, 750 °C, 900 °C, 1100 °C and 1400 °C.

TABLE I Matrix compositions and fabrication conditions used to prepare the composite samples. HT50, colloidal silica, average particle size 125 nm; X30, colloidal silica, average particle size 25 nm; CMA6, glass-ceramic system of cordierite ($5SiO_2 - 2Al_2O_3 - 2MgO$) + CaO

	Sample designation	
	HC	XQ
Matrix composition wt %	50% HT50 25% dried silica 25% CMA6	48% X30 14% dried silica 38% quartz

2.2. Microstructural analysis

Composite samples were sectioned with a diamond saw and mounted in cold-curing epoxy resin. Because of their porous nature, the composites were infiltrated under vacuum and subsequently cured under pressure in order to force the mounting resin into the pores. Mounted samples were ground flat on 240 grit silicon carbide paper, finely ground with a 9 μm oil-based diamond slurry and finally polished with a 1 μm diamond slurry and a 50 nm silica suspension. Optical microscopy was carried out in reflected light with Nomarski differential interference contrast (DIC) and dark-field modes on a Zeiss ICM 405 microscope. The polished samples were sputtered with a thin layer of gold for analysis in a scanning electron microscope (SEM), a Jeol JSM 35C fitted with a Link AN10000 energy-dispersive X-ray spectrometer (EDS). Fracture surfaces and polished sections through fractured specimens were also prepared and analysed in this manner.

Thin sections (approximately a few hundred nanometres thick) suitable for transmission electron microscopy (TEM) were prepared by cutting 3 mm

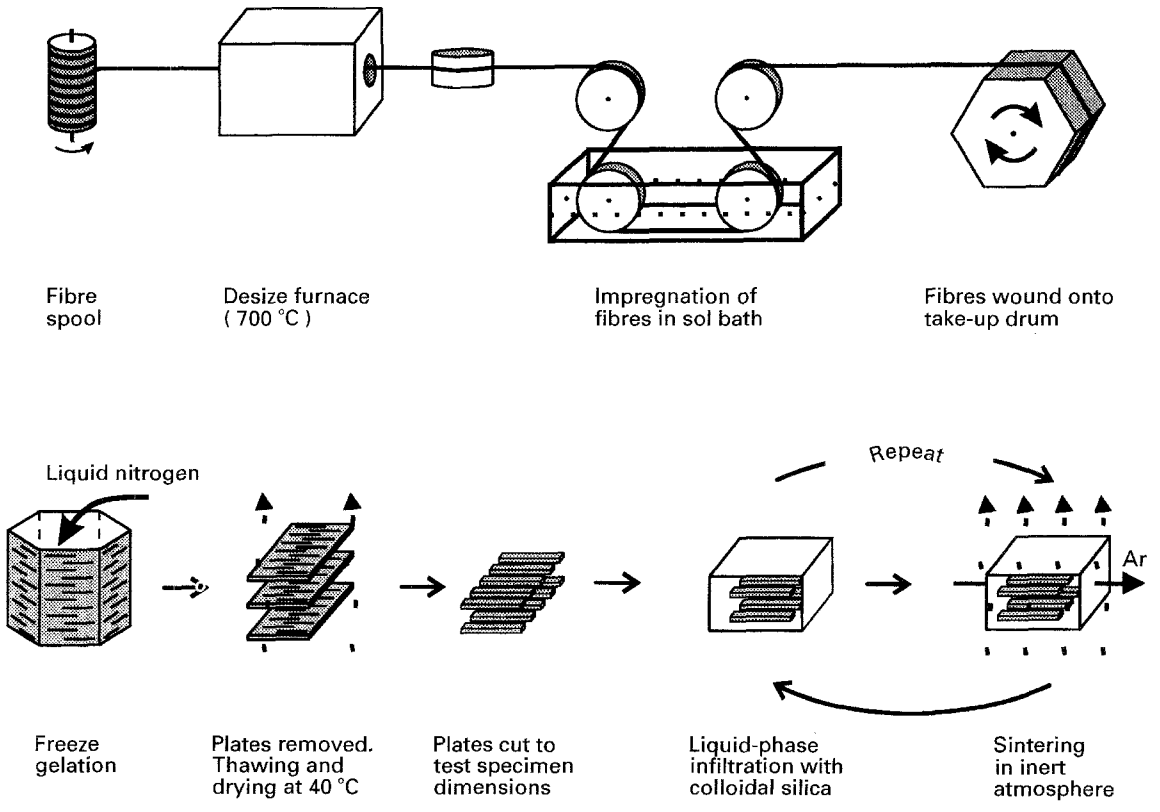

Figure 2 Outline of the filament winding route used to prepare samples.

discs with a hollow, diamond-tipped drill, mechanically grinding them to a thickness of $\sim 300\ \mu m$ and dimpling them to leave a central region $\sim 10\ \mu m$ thick. Thinning with argon ion bombardment in a Gatan Duomill was then carried out until specimen perforation occurred. TEM analysis was performed in a Jeol 2000FX equipped with an EDS system.

A sample of T300 carbon fibre and small pieces of each composite sample were ground into a fine powder for examination by X-ray diffraction (XRD) in a Philips model 1820 diffractometer.

2.3. Mechanical property characterization

Three-point bend testing was used to characterize the mechanical responses of the specimens, and provide an indication of elastic modulus, of strength and of "toughness". Testing was performed on an Instron 1195, all data being acquired by a digital data acquisition system for storage and subsequent analysis. Span-to-depth ratios of between 25 and 35 were used. Elastic moduli were calculated from the initial, linear regions of force/displacement curves using a linear regression method. Standard beam-bending equations were used to calculate peak strengths and moduli [12]. Integration of force/displacement curves gave work of fracture (WOF)-type results; the areas under the curves were divided by twice the specimen cross-sectional area to give crude indicators of toughness.

Ultrasonic moduli were determined by a time-of-flight method. Specimens were ground flat and square, and the shortest time taken for a 150 kHz pulse to travel the length of each specimen was measured with a digital monitor. Vaseline was used as a coupling agent between the specimens and the send/receive transducers. From the wave speeds, c, the longitudinal dynamic moduli, E_{dyn}, were calculated by the application of the approximate relationship $E_{dyn} = \rho c^2$, where the specimen densities, ρ, were determined by dimension measurement followed by weighing.

3. Results

3.1. Microstructural evaluation

3.1.1. Composite series "HC" (amorphous silica and glass-ceramic filler)

XRD spectra from the ground powders of composites sintered at 750 and 1100 °C are given in Fig. 3. The sample sintered at 750 °C appeared to be almost wholly amorphous, with no evidence of peaks attributable to crystalline material. Increasing the sintering temperature led to an increased degree of crystallinity. Thus, for samples sintered at 1100 °C, two crystalline phases were identified, namely anorthite ($CaO \cdot Al_2O_3 \cdot 2SiO_2$) and α-cristobalite ($SiO_2$). Even at this higher sintering temperature, however, the composite still contained appreciable amounts of amorphous material.

Composite samples were slightly non-planar and exhibited non-uniform thickness. The colour of the matrix changed from white to blue as the sintering temperature was increased beyond 1100 °C. Fig. 4a,

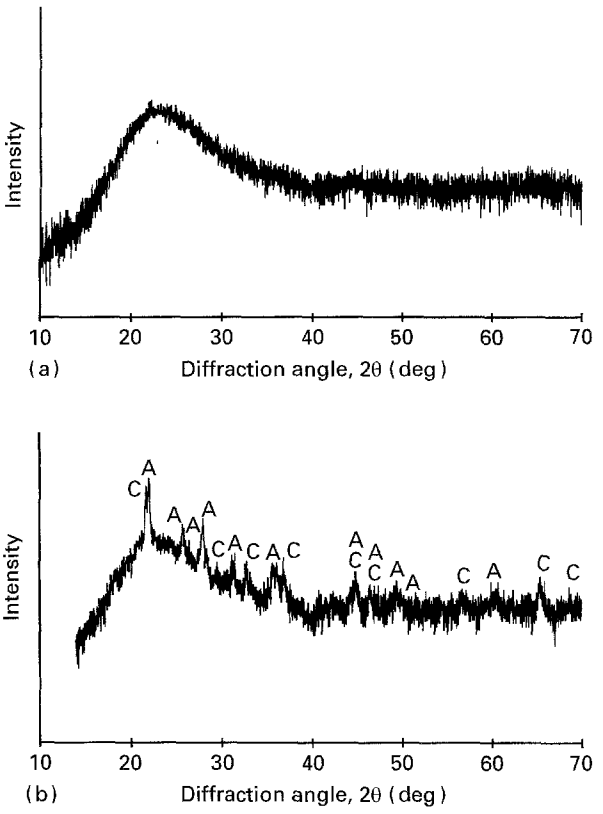

Figure 3 XRD spectra of sample HC following sintering at (a) 750 °C and (b) 1100 °C. A, anorthite; C, α-cristobalite.

an optical micrograph of a sample sintered at 750 °C, shows an extensive network of porosity. There are several discrete layers across the width of a sample. Commencing from the surface where freeze gelation began (top of Fig. 4a), one sees a fibre-free, dense layer at the outer surface, below which is a region of coarse, highly directional porosity. This porosity, of the order of ~ 30–$50\ \mu m$ in width, appears to follow the direction of heat flow during the freeze gelation process and closely resembles the columnar crystallization patterns observed in chilled metallic ingots. This columnar porosity was observed in both planes perpendicular to the fibres. There is then a reasonably well-densified region, and a region of fine, dendritic-like porosity in the centre where volume fractions of porosity of over 50% have been observed.

A sample sintered at 1400 °C, Fig. 4b, does not show this layered porosity to the same extent, although the directionality of the columnar porosity is still evident. As a general trend, an increase in sintering temperature led to a decrease in the overall degree of porosity and to a slightly enhanced degree of matrix densification near to the specimen surfaces, although no explicit relationship between degree of porosity and sintering temperature was established. Sintering temperature did not affect bulk density, which remained constant at $\sim 1.38 \times 10^3\ kg\ m^{-3}$, presumably because the method of measuring density was insufficiently sensitive to detect porosity effects.

Dark-field illumination in the optical microscope revealed the pores to have a crystalline surface texture, and more readily distinguished between the denser (darker) and more porous (lighter) regions of the specimens. Also, a degree of subsurface detail is revealed.

Fibre distribution was non-uniform in all samples. The variations seen between individual samples made it difficult to draw definite conclusions, but generally the fibres were better dispersed in the denser matrix regions, typically nearer to the edges of specimens. Fibres were often seen bundled in their original tows, frequently on the plane adjacent to a particularly porous region. Fibre volume fraction was estimated to be between 0.10 and 0.15 for all specimens (estimates were obtained by controlled pyrolysis of carbon fibres and by image analysis of polished transverse sections).

Matrix cracks arising from residual stresses were observed in all samples, and these tended to reach the specimen surface via dense matrix regions. Regularly spaced transverse cracks were seen in dense, internal matrix layers, although their presence was obscured frequently and interrupted by porosity (Fig. 5). The spacing of these cracks ranged from 1000 μm for samples sintered at 900 °C and below, to 200–400 μm for samples sintered at 1100 °C and above. Matrix cracking around fibres was also seen. Fig. 6 shows typical cracking in a sample sintered at 1100 °C, the circumferential crack pattern being indicative of residual

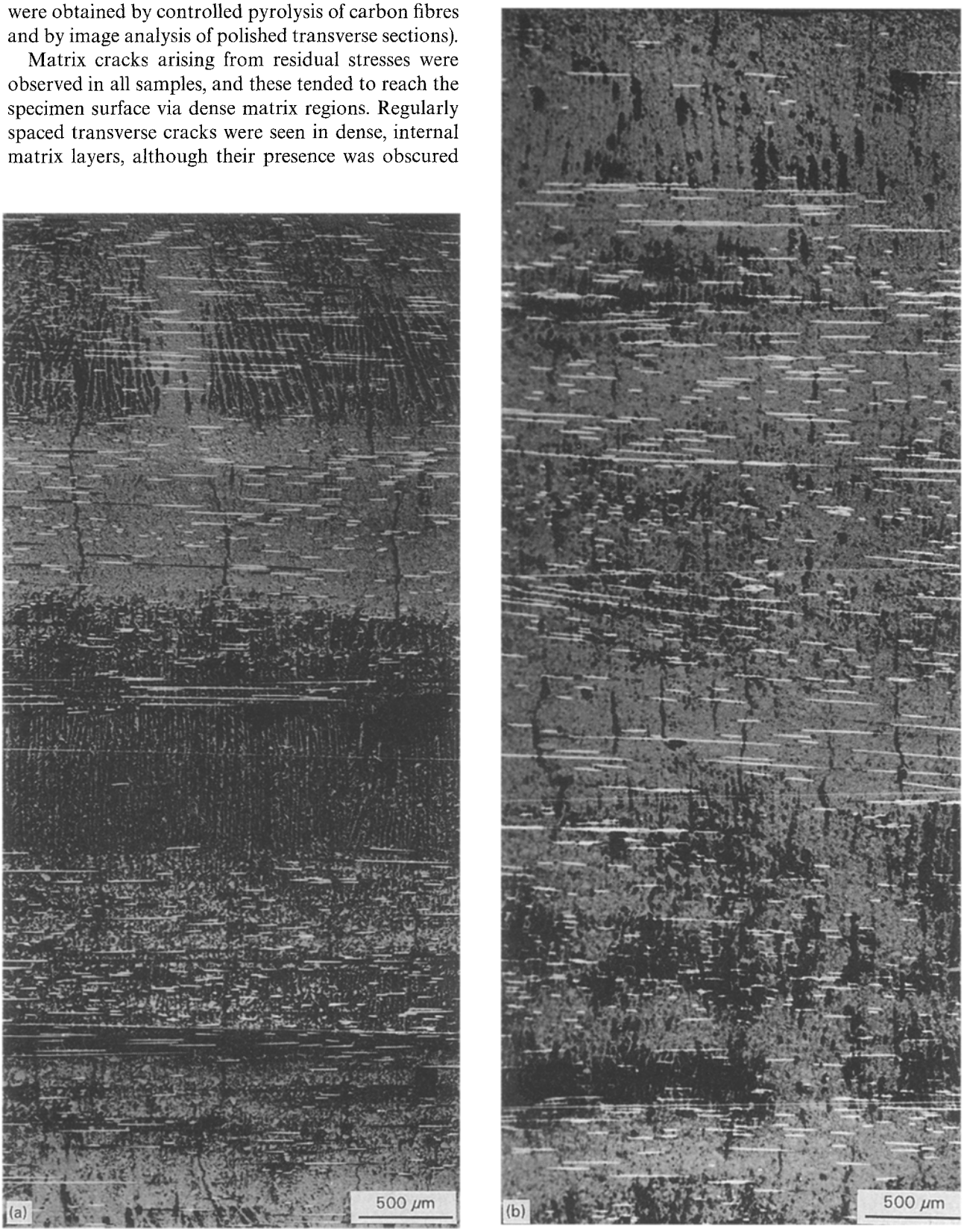

Figure 4 Optical (DIC) micrographs of transverse sections of sample HC sintered at (a) 750 °C and (b) 1400 °C. The top edges of these micrographs were in contact with the mandrel during freeze gelation.

Figure 5 Example of transverse matrix cracking in dense matrix layer of as-received sample.

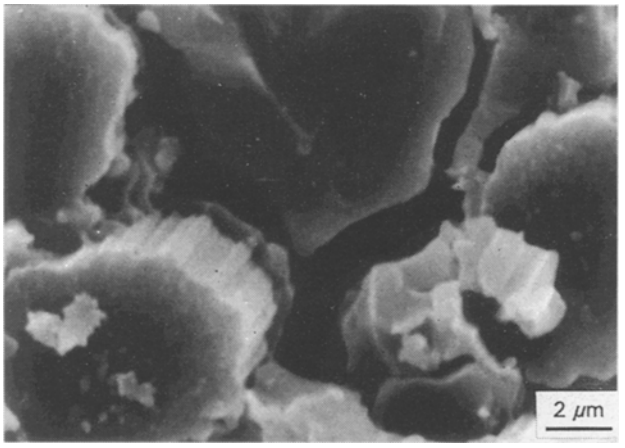

Figure 6 Circumferential matrix cracking around a fibre arising from residual stresses.

stresses arising from fibre/matrix thermal expansion mismatches.

SEM of polished samples revealed the multiphased nature of the composite matrix. Fig. 7a is from a sample sintered at 900 °C. EDS indicated that the higher particles (P1) and the sol–gel matrix consisted of silicon and oxygen (Fig. 7b), whilst the darker particles (P2) contained silicon, oxygen, aluminium, magnesium, calcium and titanium (Fig. 7c). After sintering at 1100 °C the large, interconnected porosity was still present, and many of the larger filler particles were cracked internally (Fig. 7d).

Fig. 8a, a transmission electron micrograph from a sample sintered at 900 °C, shows a filler particle (labelled P) and a region of sol–gel derived silica matrix (M). The sol–gel region consisted of agglomerated silica spheres up to 140 nm diameter and many small pores of nanometre scale. Selected-area diffraction (SAD) showed both phases to be amorphous and EDS indicated that silicon, oxygen, aluminium, magnesium, calcium and titanium were present in the filler and only silicon and oxygen in the sol–gel matrix. A second type of filler particle was found to be amorphous and to contain only silicon and oxygen.

After sintering at 1100 °C, changes in the matrix were observed. SAD showed that the calcium- and magnesium-containing particles had become partially crystallized (Fig. 8b), to form a lath-like crystal phase, although it was not possible to identify this phase. The silica filler particles also appeared to have crystallized in some areas; Fig. 8c illustrates a crystalline region confirmed as being α-cristobalite by SAD. The surrounding sol–gel matrix remained amorphous.

The interface between the carbon fibre and the surrounding matrix in the sample sintered at 1100 °C is shown in Fig. 8d. Debonding was observed along the interface, indicating that the interfacial bond between the sol–gel region and the fibre was weak.

3.1.2. Composite series "XQ" (amorphous silica and quartz filler)

The XRD traces from powdered samples sintered at 750 °C, Fig. 9a, exhibited a series of crystalline peaks, identified as α-quartz, and some amorphous material. The composite sintered at 1100 °C (Fig. 9b) showed in addition a series of peaks which were identified as α-cristobalite, together with a corresponding reduction in the amorphous content.

The overall appearance of the samples was similar to that reported for the HC series composites, i.e. non-planar and not uniformly thick. The effect of sintering temperature on the form and degree of porosity was similar to that summarized in Fig. 4 for the HC series. Increasing the sintering temperature resulted in reduced visible porosity, although once again no quantitative relationship could be found between levels of porosity and sintering temperature. Sample density was $\sim 1.41 \times 10^3\ \mathrm{kg\,m^{-3}}$ for all sintering temperatures.

SEM analysis revealed a non-uniform fibre distribution. In composites sintered between 600 and 900 °C, cracking in the sol–gel matrix and residual porosity were identified and filler particles were discernable (see Fig. 10a, taken from a sample sintered at 900 °C). Sintering at 1100 °C changed the appearance of the microstructure (Fig. 10b): filler particles were no longer distinguishable in the matrix, and the matrix itself was extensively cracked in the fibre-free regions. Where fibre density was high, cracking was present but on a finer scale. EDS indicated the presence of silicon and oxygen in the matrix constituents.

TEM studies of the composite sintered at 900 °C showed that the originally spherical particles began to form a fused network (Fig. 11a). At lower magnifications (Fig. 11b), quartz filler particles (Q) were seen, as well as regions where matrix crystallization had commenced (C). This matrix crystallization had proceeded to completion in the specimen sintered at 1100 °C, Fig. 11c. In this micrograph a quartz filler particle (Q) is seen in a crystalline matrix (C). The filler particle

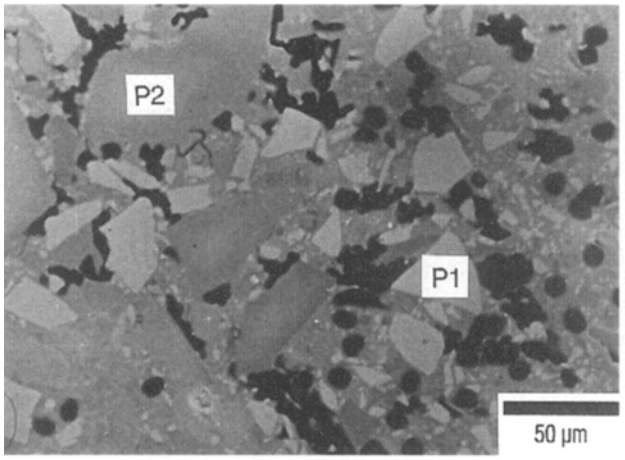

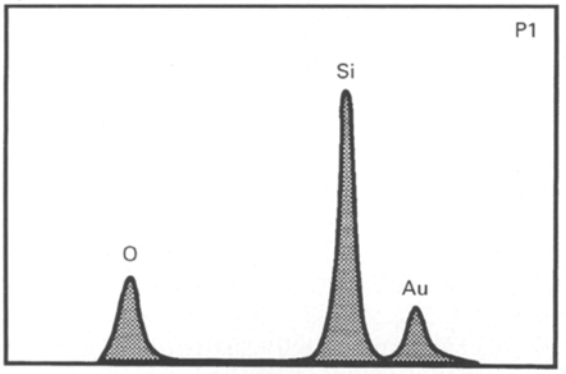

(b)

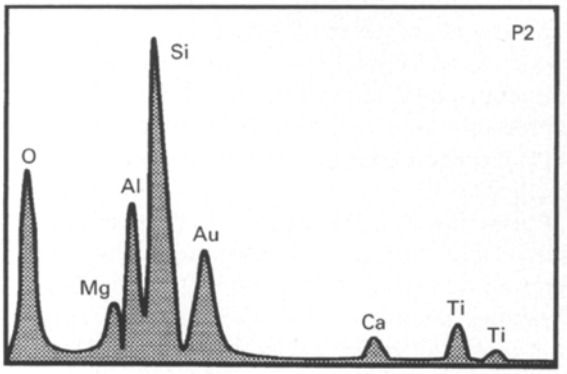

(c)

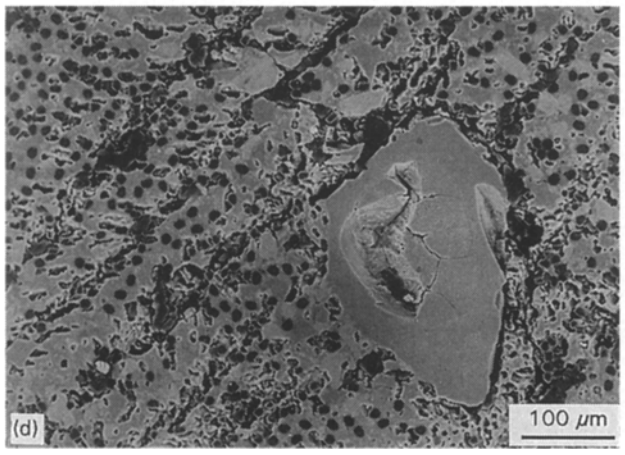

Figure 7 (a) Scanning electron micrograph of a polished, transverse section of sample HC sintered at 900 °C; (b, c) EDS traces of particles P1 and P2 as marked. (d) Scanning electron micrograph of sample HC sintered at 1100 °C showing matrix porosity and internal cracking of a filler particle.

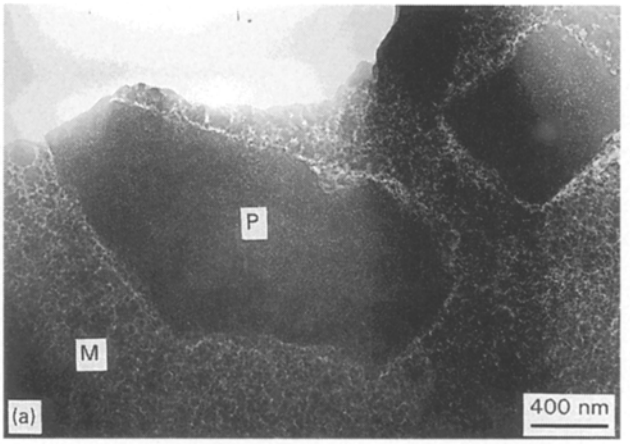

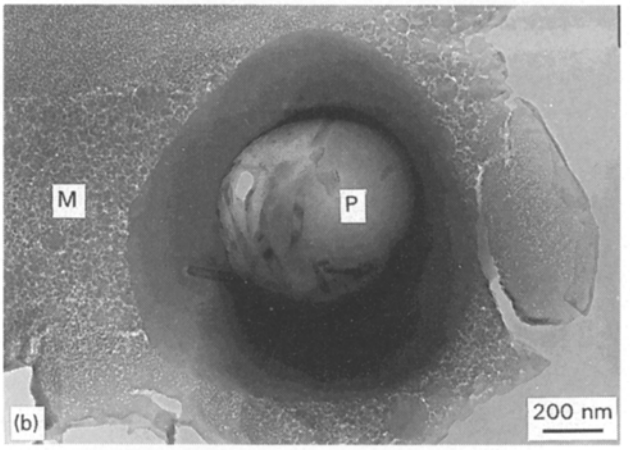

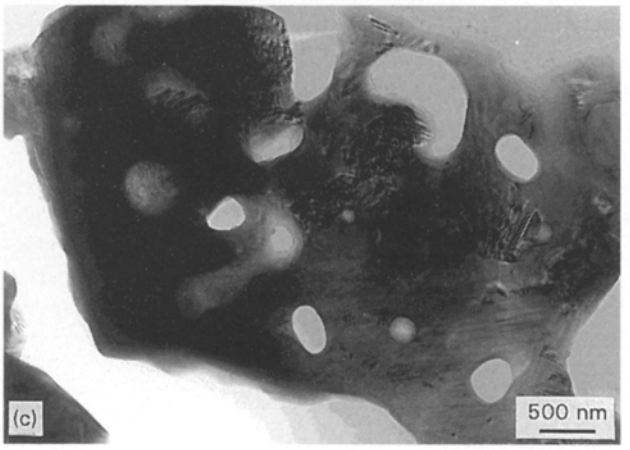

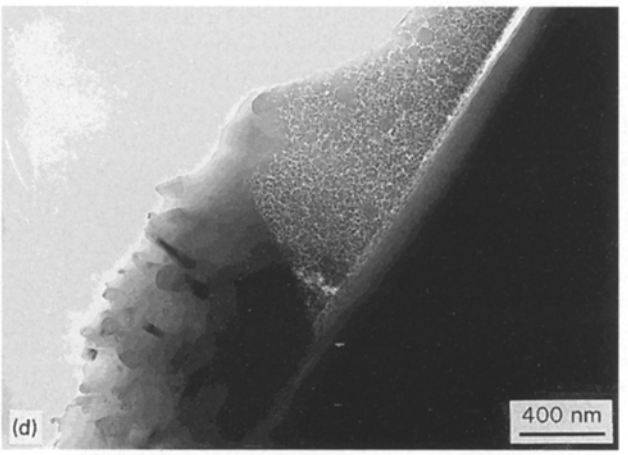

Figure 8 (a) Transmission electron micrograph of sample HC sintered at 900 °C; (b) transmission electron micrograph of sample HC sintered at 1100 °C (P, filler particle; M, sol–gel silica matrix); (c) region of cristobalite in filler particle P; (d) transmission electron micrograph of fibre/matrix interface in sample HC sintered at 1100 °C.

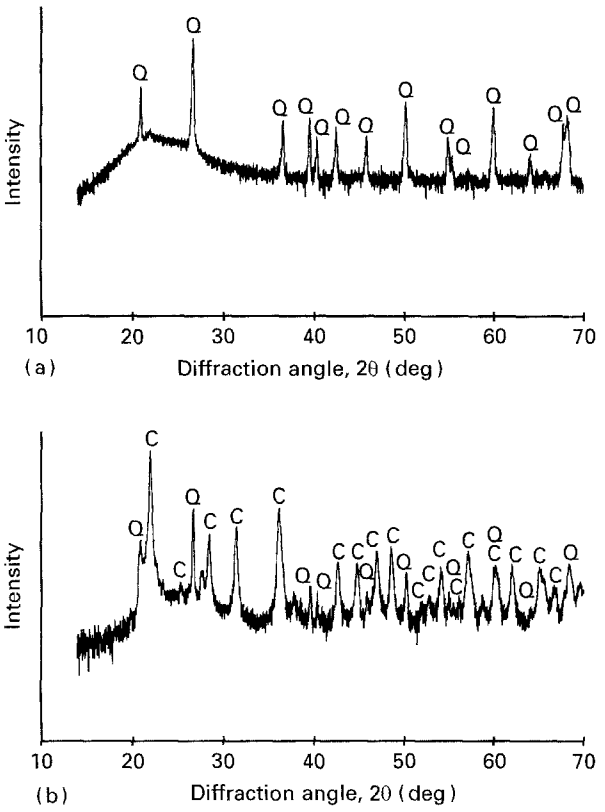

Figure 9 XRD spectra of sample XQ following sintering at (a) 750 °C and (b) 1100 °C. C, α-cristobalite; Q, α-quartz.

exhibited strain bands and the matrix contained several twinned regions, both suggestive of residual strains within the material. SAD confirmed that the filler particle was α-quartz, and that α-cristobalite was present in the sol–gel matrix region. Closed porosity of the order 0.1–2 μm in size was also visible in the matrix. As with the HC samples, residual stresses caused matrix cracking around fibres. Transverse matrix cracking was also observed, the crack-spacing/temperature relationships being similar to those reported for the HC samples.

3.2. Mechanical test results

Figs 12 and 13 summarize the flexural mechanical properties and dynamic moduli obtained for the HC and XQ series, respectively. These show the variation of (a) peak stress, (b) flexural and dynamic elastic moduli, and (c) "work of fracture" (WOF) with sintering temperature. Error bars indicate coefficients of variation; where no bars are shown, it may be assumed that the errors are of the same magnitude as the datum point markers. Figs 14 (HC) and 15 (XQ) are typical force/displacement curves obtained during flexural testing for samples sintered at (a) 600 °C, (b) 900 °C and (c) 1400 °C. More detailed features of the HC and XQ mechanical test results are now discussed, followed by an overview of damage evolution and fracture processes in both series of materials.

3.2.1. Composite series "HC" (amorphous silica and glass-ceramic filler)

Peak stress values were ~ 150 MPa for all sintering temperatures. The elastic modulus increased with sintering temperature, particularly beyond 900 °C, to reach a maximum value of 15 GPa (mechanical) or 20 GPa (dynamic). The difference between the dynamic moduli and the mechanically derived moduli became greater as sintering temperature was increased; the ratio between dynamic and flexural moduli, $E_{dyn}:E_{mech}$, was ~ 1.4.

Work of fracture showed a sharp drop at a sintering temperature of 900 °C, falling from ~ 6 kJ m^{-2} to ~ 2 kJ m^{-2}. This sudden reduction in toughness is reflected in the form of the force/displacement curves, Fig. 14, and in the macroscopic appearance of the fractured specimens (Fig. 16). The tensile fracture surface of a sample sintered at 750 °C, Fig. 17a, exhibits appreciable fibre pull-out, whilst fibre pull-out was much more restricted in the sample sintered at 1100 °C (Fig. 17b).

Furthermore, SEM analysis indicated that fibre/matrix bond strength was enhanced as sintering temperature was increased beyond 900 °C. Fig. 18a, from a sample sintered at 900 °C, shows an unbonded fibre/matrix interface where the relative cleanness of the fibre indicates little, if any, fibre/matrix adhesion. In contrast, Fig. 18b, from a sample sintered at 1400 °C, shows a fibre/matrix interface which is in the process of being debonded.

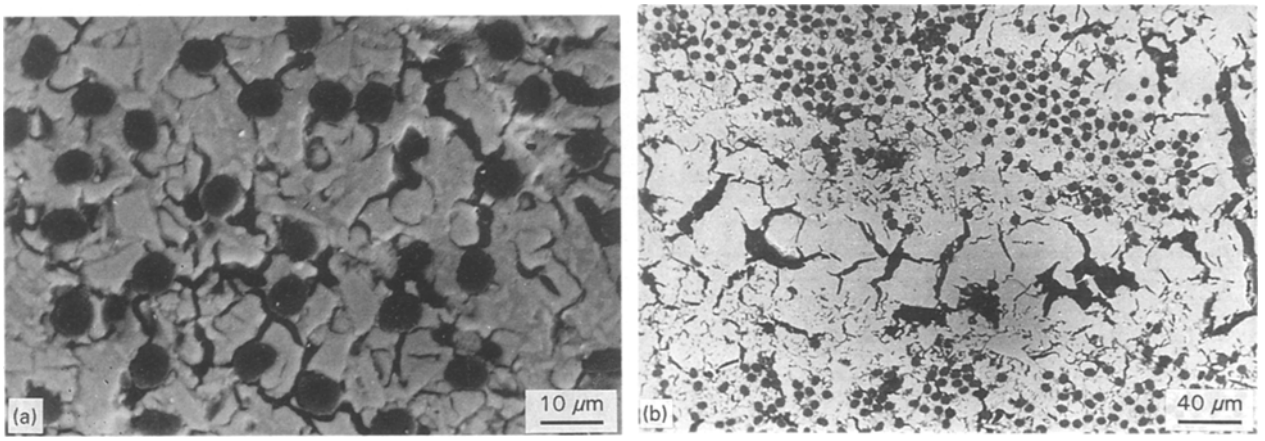

Figure 10 Scanning electron micrographs of sample XQ following sintering at (a) 900 °C and (b) 1100 °C.

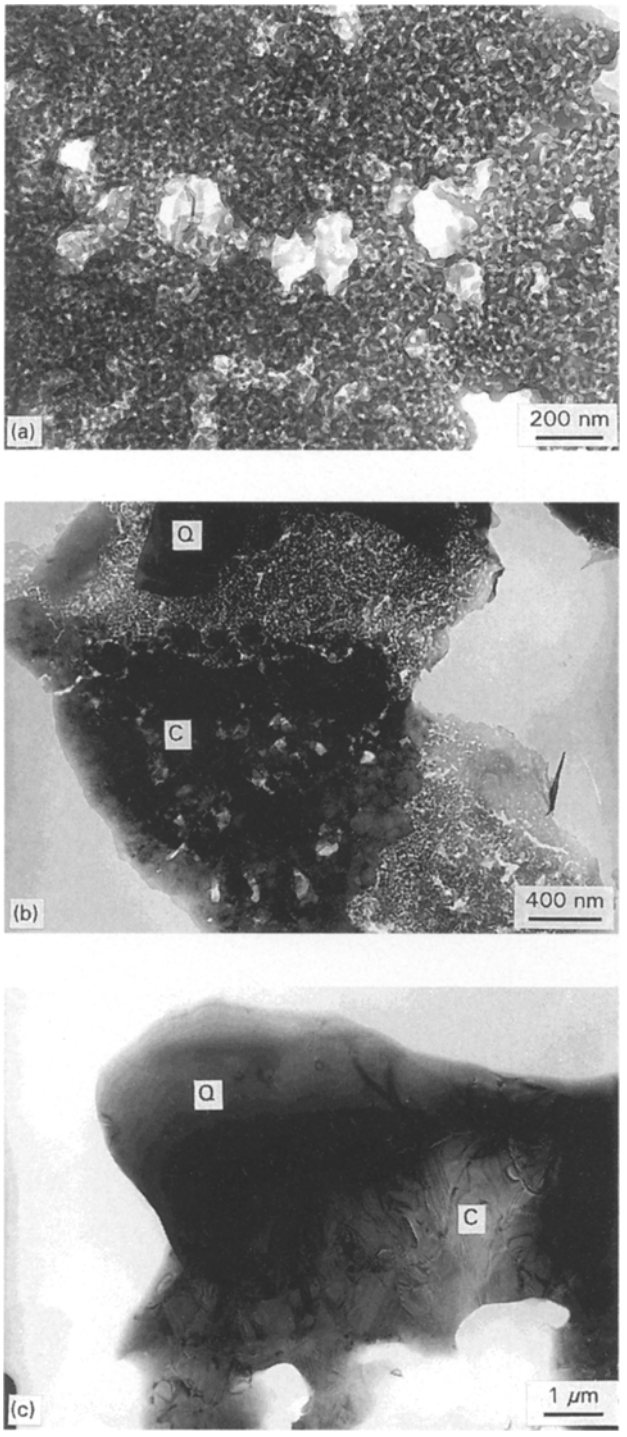

Figure 11 Transmission electron micrographs of sample XQ sintered at (a) 900 °C showing the initially spherical silica particles beginning to fuse (quartz filler particles, Q, and regions of matrix crystallinity, C, can be seen in (b)), and (c) 1100 °C.

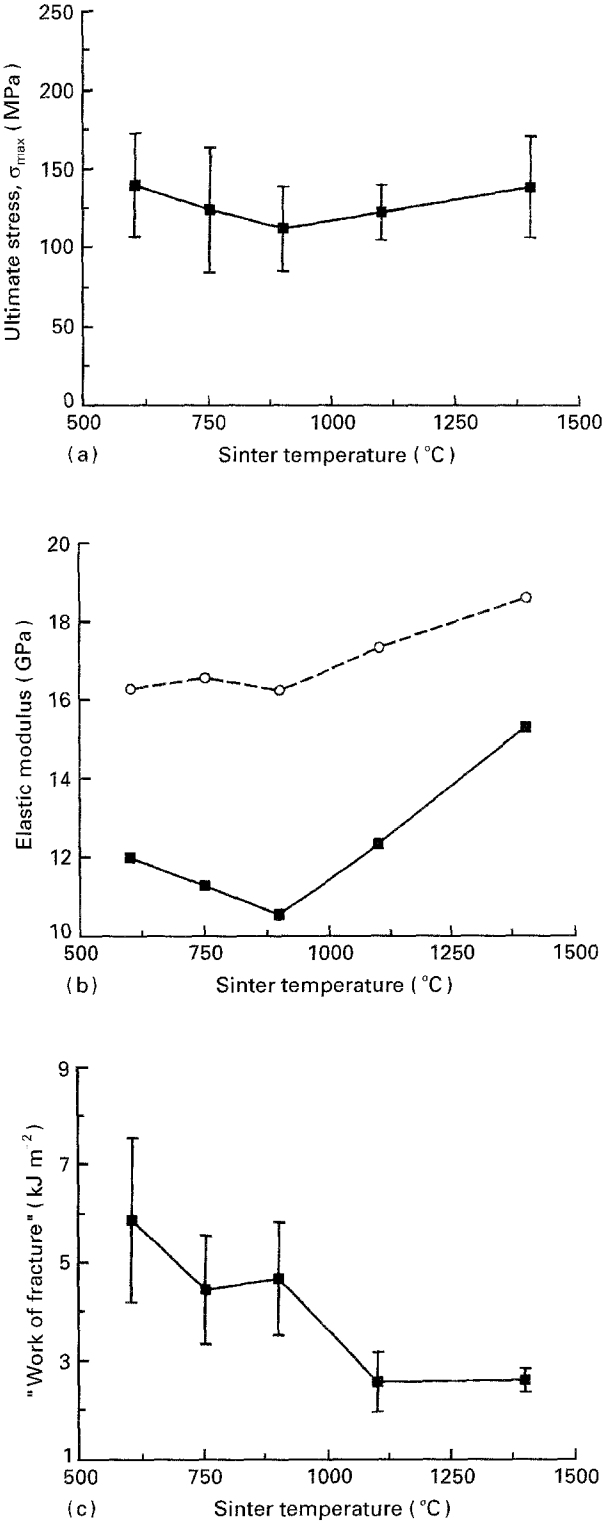

Figure 12 Sample HC: variation of (a) peak stress, (b) (——) flexural and (– – –) dynamic elastic moduli and (c) "work of fracture" (WOF) with sintering temperature.

3.2.2. Composite series "XQ" (amorphous silica and quartz filler)

Peak stress levels were ~ 200 MPa for samples sintered at 600 and 750 °C (Fig. 13) and decreased to ~ 100 MPa for samples sintered above 750 °C. The flexural modulus decreased gradually from ~ 18 GPa (600 °C sinter) to ~ 14 GPa for samples sintered at 1400 °C. Dynamic moduli were again consistently higher than the equivalent mechanical moduli, with $E_{dyn}:E_{mech}$ varying between 1.2 and 1.4. With the exception of a possibly anomalous datum point at 750 °C, dynamic moduli decreased very gradually with increasing sintering temperature.

Work of fracture showed a very pronounced decrease beyond 750 °C, falling from ~ 8.5 kJ m^{-2} to 1.5 kJ m^{-2}. As with the HC composites, these trends were reflected in the form of the force/displacement curves (Fig. 15), and in the overall appearance of the fractured samples, i.e. minimal fibre pull-out for samples sintered at high temperatures and extensive fibre pull-out for samples sintered at lower temperatures.

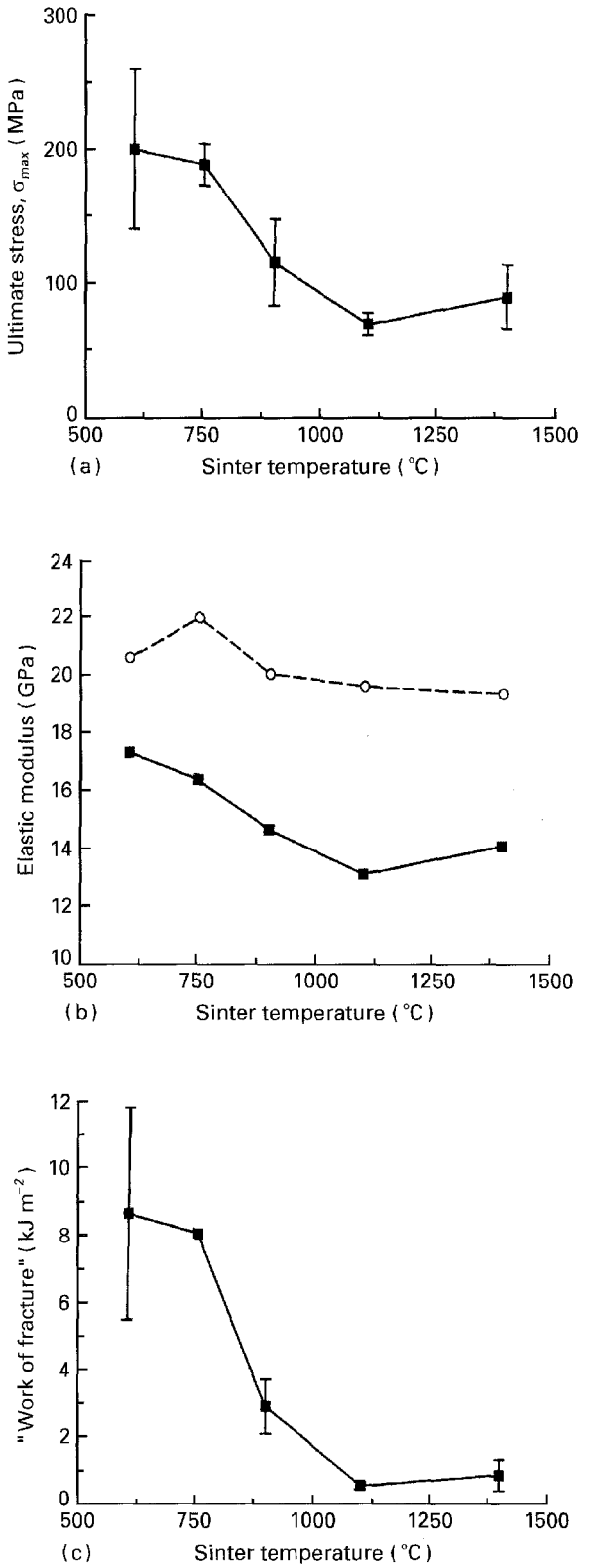

Figure 13 Sample XQ: variation of (a) peak stress, (b) (——) flexural and (– – –) dynamic elastic moduli and (c) "work of fracture" (WOF) with sintering temperature.

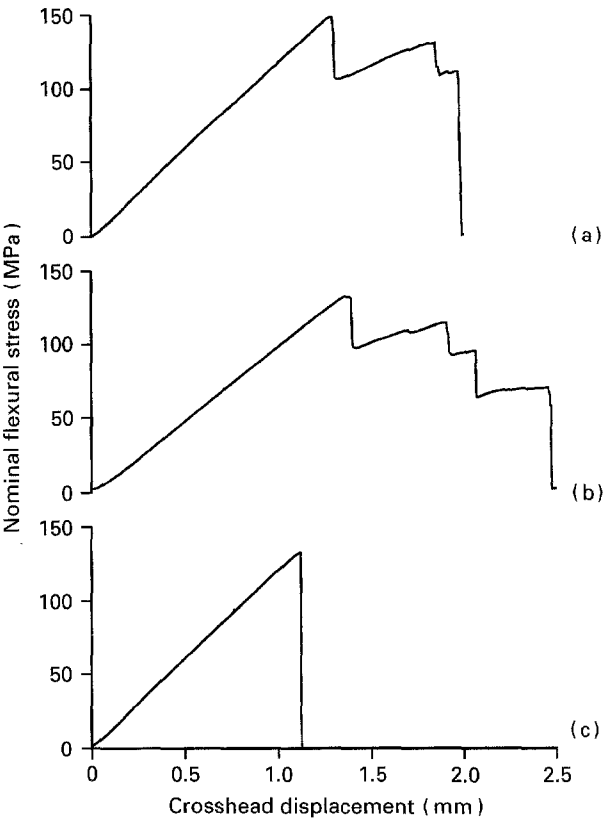

Figure 14 HC series: typical force/displacement curves obtained during flexural testing for samples sintered at (a) 600 °C, (b) 900 °C and (c) 1400 °C.

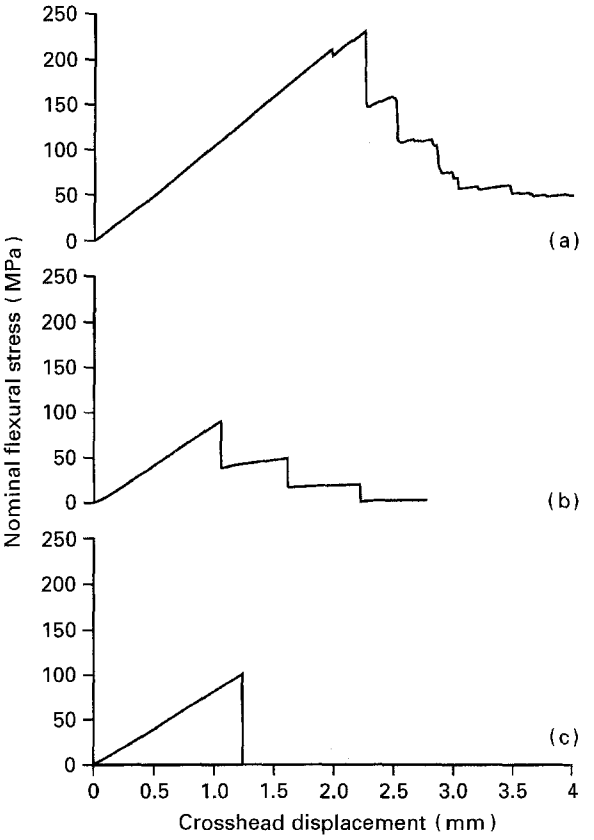

Figure 15 XQ series: typical force/displacement curves obtained during flexural testing for samples sintered at (a) 600 °C, (b) 900 °C and (c) 1400 °C.

3.2.3. Damage processes

Several factors contributed to the difficulty in identifying and classifying the fracture mechanisms active in these samples. These include complex porosity patterns and fibre distributions, non-uniformity of the test specimens, and the resultant complex stress states under flexure (which change in the course of a test), all of which vary between individual specimens. However, some features common to the damage behaviour of all the samples may be noted.

Fig. 19 schematically shows the two different types of crack-growth behaviour which were observed. For

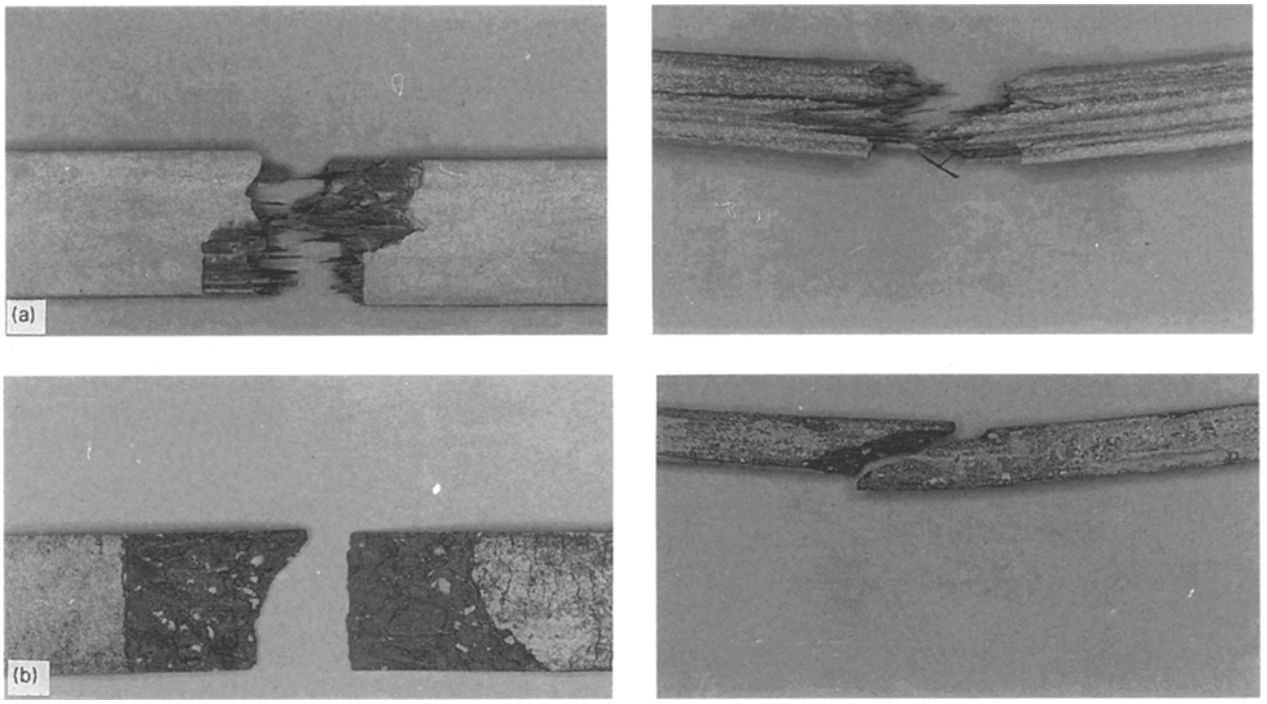

Figure 16 Macro view of fracture surfaces of HC samples sintered at (a) 750 °C and (b) 1400 °C. Specimen width is 10 mm in all cases.

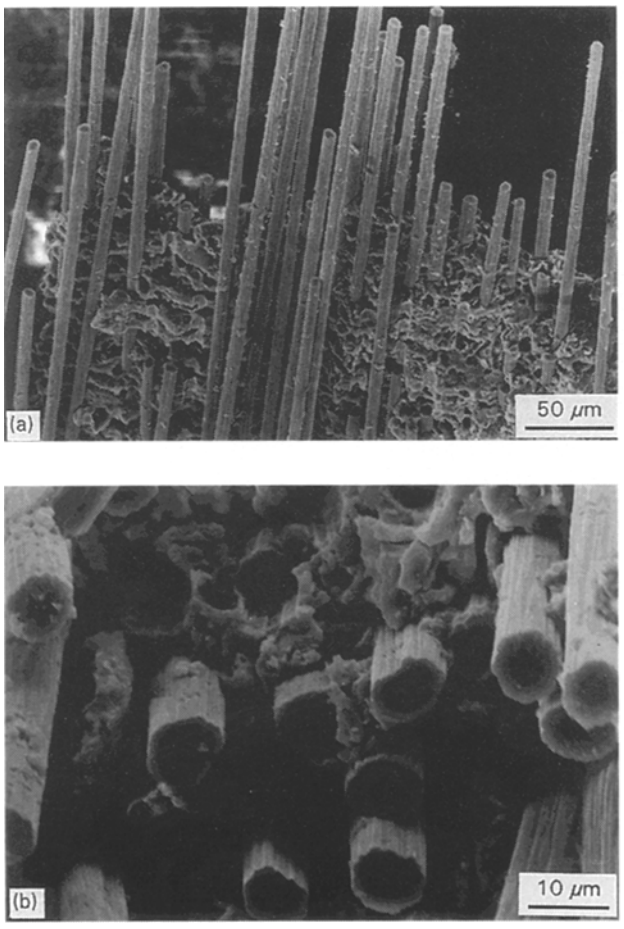

Figure 17 Scanning electron micrographs of fracture surfaces (tensile side) of HC samples sintered at (a) 750 °C and (b) 1100 °C.

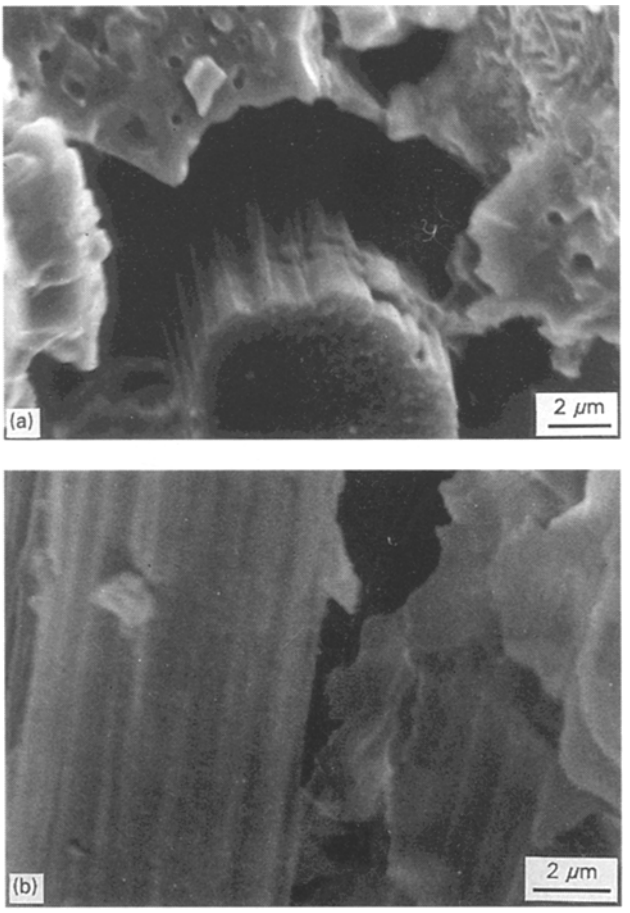

Figure 18 (a) Low fibre/matrix bond strength in sample sintered at 900 °C; (b) high fibre/matrix bond strength in sample sintered at 1400 °C: a debonding interface is shown.

samples sintered at 1100 °C and above, Fig. 19b, the primary crack initiated from the tensile face of the specimen and passed cleanly into the body of the specimen, with minimal crack deflection via delamination-type events. Very little fibre pull-out was observed.

A much tougher mode of failure was seen with samples sintered at lower temperatures (900 °C and

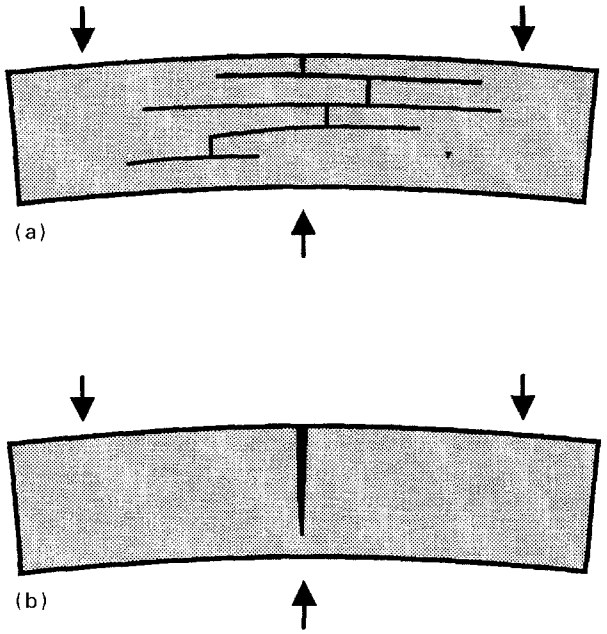

Figure 19 Schematic representation of flexural damage behaviour in (a) tough and (b) brittle composites. (a) and (b) correspond to sintering temperatures 600–900 °C and above 1100 °C, respectively.

below), as demonstrated by the change in form of the force/displacement curves and the appearance of the fracture surfaces. Growth of the primary crack again occurred perpendicular to the fibres, Fig. 19a, apparently following the columnar porosity patterns described earlier. A form of delamination then took place much earlier than seen for the samples sintered at higher temperatures; this crack deflection was often accompanied by fibre and/or ligament bridging. Tensile opening faces were accompanied by significant degrees of fibre pull-out (as described in the preceding sections). Delamination cracking coincided with the sudden load drops in the force/displacement curves, and the reloading moduli of the curves decreased with each major cracking/delamination event

These descriptions simplify what is evidently a very complex damage process and have not attempted to deal with the roles of the different types of porosity in influencing crack growth. Indeed there were cases where the initiation and growth of matrix cracks could be attributed to or associated with porosity. Fig. 20a, for example, illustrates the beginning of a pore link-up leading to fibre debonding (Fig. 20b) and, ultimately, to the form of crack shown in Fig. 20c. In other cases regions of porosity "absorbed" cracks.

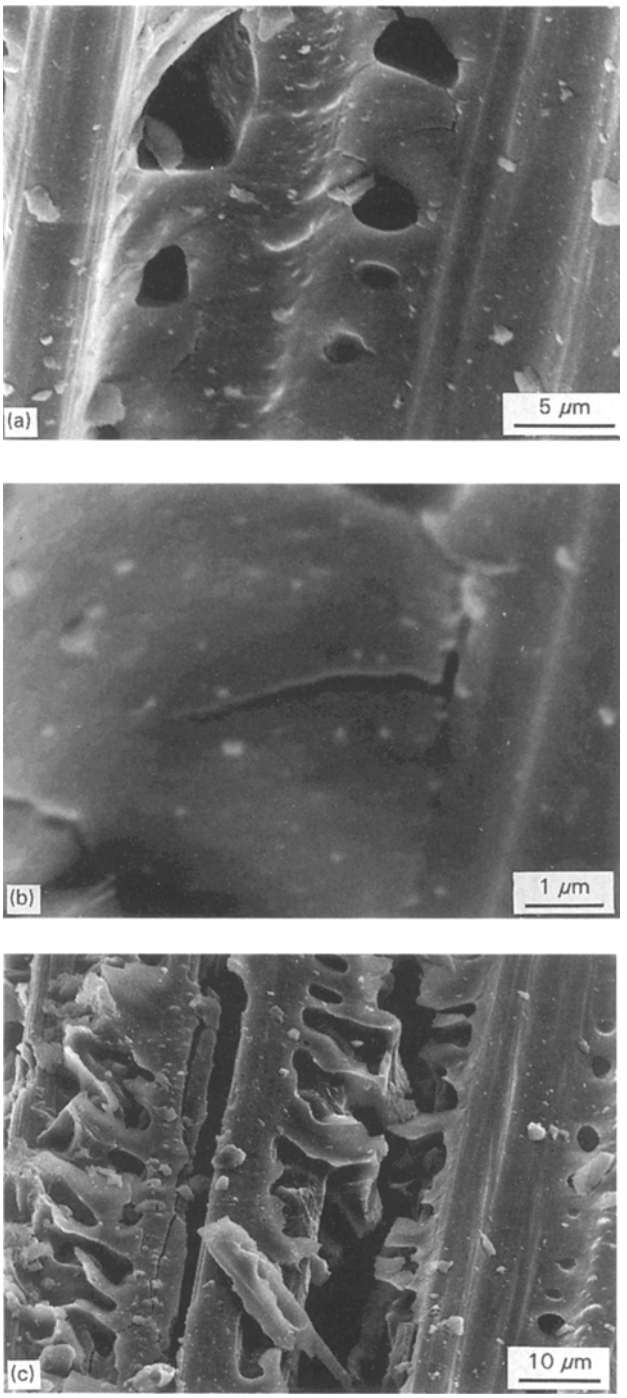

Figure 20 Matrix porosity may link up (a) and lead to early debonding at the fibre/matrix interface (b). Following testing to failure, the type of damage shown in (c) is observed, with extensive porosity link-up and matrix splitting parallel to the fibres.

4. Discussion

4.1. Microstructural evaluation

The freeze gelation process gives rise to distinctive patterns of porosity within the composite samples. Several types of gross porosity can be identified on a micrometre scale, and nanometre scale porosity is present between the colloidal particles of the silica sol–gel matrix. Whilst the details of these porosity patterns are obscured frequently by the effects of infiltration and subsequent sintering, it is apparent that the large uninfiltrated pores occupy the regions where ice crystals grew during the freeze gelation step. In order to understand the development of the complex porosity patterns in these materials, one therefore needs to consider the mechanisms of growth of the ice crystals during the freeze gelation process and how these original pores were filled by the subsequent liquid-phase infiltration and sintering steps.

When liquid nitrogen is poured into the hollow mandrel, there is initially a very high temperature gradient across the thickness of the wet composite samples. Coarse, columnar ice crystals grow in the direction of the temperature gradient (i.e. perpendicular to the fibres) to a depth of ~ 2 mm. The colloidal

silica and filler particles are squeezed into the regions between the ice crystals and will eventually form the matrix of the composite. As the ice growth front extends, the temperature at the head increases and the temperature gradient therefore decreases. The ice crystals become less directional and this leads to an observed region of dendritic-like porosity in the composite matrix which extends to the other side of the sample. During liquid-phase infiltration, the coarse, directional pores provide little resistance to the infiltrant. The central region of fine, dendritic porosity, however, presents more of an obstacle and is only partially infiltrated. The possibility of filtration effects blocking open porosity near the outside of samples and preventing densification of the central region should be considered.

These features are seen most clearly in samples which are sintered at temperatures up to 900 °C and which exhibit clearly-defined layers of porosity. Fig. 4a, for example, shows a region of coarse (~ 30–50 μm), columnar porosity perpendicular to the fibres at the edges of the sample, followed by a reasonably well-densified layer and, in the centre of the specimen, an extensive network of open dendritic porosity.

The second major processing variable is sintering temperature. As a general trend, higher sintering temperatures gave rise to wider dense layers in the samples, although porosity was still very much in evidence and only very small changes in bulk density were measured. The influence of matrix phase changes during sintering on microstructural features and mechanical properties are discussed below.

4.1.1. Composite series "HC" (amorphous silica and glass-ceramic filler)

Composite HC samples remained amorphous when sintered at temperatures of 900 °C and below, with no evidence of crystallinity in either the sol–gel matrix or the silica and CMA6 filler particles. In contrast, composites sintered at 1100 °C and above contained two crystalline phases (α-cristobalite and anorthite); the amorphous material detected may be attributed to the carbon fibres and to the colloidal silica matrix. The α-cristobalite (SiO_2) phase is believed to have been formed by the crystallization of the silica filler during sintering, possibly growing to form the gross, internally cracked phase, whilst the anorthite ($CaO \cdot Al_2O_3 \cdot 2SiO_2$) is thought to be associated with the CMA6 glass-ceramic particles because these particles remain amorphous up to 900 °C and crystallize during sintering at 1100 °C and above. EDS identified calcium, silicon, aluminium, magnesium, titanium and oxygen in these CMA6 particles and calcium, aluminium, silicon and oxygen in the anorthite. The remaining elements (magnesium and titanium) are probably present in the glassy phase found by SAD in the TEM.

The titanium is believed to have been introduced as TiO_2 into the CMA6 as a nucleating agent for the anorthite crystals; its application in such glass-ceramic systems has been previously reported [13]. The colour change of the composites from white to blue may be explained by the size and spacing of anorthite crystals being in the red light absorption range and appearing blue in reflected light. This principle is used in the colouring of glass. Full densification of the colloidal silica was not achieved, with the original spheres still visible in the TEM even at 1100 °C

4.1.2. Quartz filler (series "XQ")

Composite XQ initially contained one crystalline phase, the α-quartz used as a filler. Sintering at 900 °C led to fusing of the silica sol–gel particles into a linked network, and to the early stages of α-cristobalite formation. After sintering at 1100 °C and above the original sol–gel matrix had crystallized completely to α-cristobalite, the filler particles remaining as α-quartz.

4.1.3. Trends in microstructure

It has been seen that higher temperatures lead to greater degrees of crystallization in both the HC and XQ series composites. In the former material, this crystallization occurs in the silica and CMA6 filler particles, whereas in the latter it is the sol–gel matrix which crystallizes. One possible explanation for the XQ material crystallizing more than the HC material is that the smaller particle size of the colloidal silica used in fabricating of the XQ composites gives rise to a higher surface area and hence an increased surface energy, providing a greater thermodynamic driving force for crystallization. However, a previously studied material which contained a quartz filler and HT50-derived silica matrix [14] exhibited very similar crystallization behaviour to XQ, i.e. α-cristobalite was formed during sintering at 1100 °C and above. Because the colloidal silica in the HC matrix did not crystallize at this temperature, some other factor must be responsible. It is, therefore, suggested that the highly crystalline quartz filler used in XQ can initiate matrix crystallization, whereas the amorphous SiO_2 and CMA6 fillers in HC cannot. This view is supported by evidence from the glass-making industry, where the presence of quartz impurities is known to cause devitrification of glass [15].

4.1.4. Residual stresses

The formation of α-cristobalite in the XQ samples and, to a lesser extent, in the HC materials has two important ramifications. Firstly, the 4% volume change on transformation from the higher temperature β-cristobalite phase to α-cristobalite inevitably sets up strains in the matrix. Some of these strains can be relieved by twinning, but the majority are dissipated by extensive matrix cracking. This matrix cracking, which is easily seen in dense matrix regions, is effectively absorbed in more porous matrix areas by sub-critical microcracking. Secondly, owing to the very large difference between the thermal expansion coefficients of colloidal silica, α-cristobalite and

carbon fibres in the radial direction ($\sim 10^{-6}$, 27×10^{-6} and $8 \times 10^{-6}\,K^{-1}$, respectively). "Clamping" of the fibres by the matrix is therefore conceivable.

The difference in thermal expansion coefficients of fibres and matrix led to observable residual stresses in the composite samples, a result of cooling from elevated sintering temperatures to ambient conditions. Phillips *et al.* [16] derived the following expression for axial residual stresses in unidirectional composites

$$\sigma_{residual} = \frac{E_f V_f(\alpha_m - \alpha_f)\Delta T}{1 + V_f(E_f/E_m - 1)} \quad (1)$$

where V_f is the fibre volume fraction, α_f and α_m are the thermal expansion coefficients of the fibre and matrix, E_f and E_m are the elastic moduli and ΔT is the temperature difference on cooling from the processing temperature to ambient. If one takes the values of these parameters given in Table II, then positive residual stresses are predicted, varying from about 13–30 MPa for sintering temperatures between 600 and 1400 °C. The tensile stresses thus generated within the matrix may be sufficient to cause matrix cracking (as has been seen in dense matrix regions) or localized matrix cracks may be deflected and absorbed in regions of fine, dendritic porosity.

Within dense matrix strata, transverse matrix cracking consistent with the form predicted by the theory of Aveston *et al.* (ACK) [17] is seen, which we believe to be the result of thermal residual stresses. These transverse cracks were generally quite regularly spaced, varying from about 1000 μm for samples sintered at temperatures up to 900 °C, to around 250 μm for samples sintered at 1100 °C and above. This was true for both the HC and XQ composites.

ACK theory predicts that saturation matrix crack spacing, x, varies with interfacial shear strength, τ, as $x \propto \tau^{-1}$. This suggests that τ(1100 °C) is around three to four times greater than τ(900 °C), and is qualitatively consistent with observed fibre pull-out lengths. Direct application of the ACK relation assumes, of course, that the levels of thermal residual stress which give rise to the matrix cracks are sufficient to cause saturation matrix cracking, which is probably an over-simplification in this case.

4.2. Mechanical properties

The problems associated with the mechanical testing of ceramic-matrix composites have been the subject of a number of reviews (see, for example, [18]). Strength and modulus measurements have generally been made by means of flexure tests similar to those employed for isotropic, monolithic ceramics because of the ease with which such measurements can be performed, despite the fact that tensile data are arguably more useful. The low shear strengths of unidirectional ceramic-matrix composites means that test geometries need to be carefully defined if shear failure is to be avoided and tensile failure encouraged during flexural testing; the ratio of loading span to beam thickness must be large, typically greater than 25.

TABLE II Fibre and matrix properties used to calculate thermal residual stresses

Matrix Young's modulus, E_m	75 GPa
Fibre Young's modulus, E_f	230 GPa
Matrix axial CTE, α_m	$1 \times 10^{-6}\,K^{-1}$
Fibre axial CTE, α_f	0
Mean fibre volume fraction, V_f	0.12

The pronounced bending and non-uniform thicknesses of the composites investigated in this study caused the samples to be unsuitable for tensile testing. Three-point bend testing was therefore used to characterize the mechanical responses of the samples, in contrast to providing definitive mechanical property data. It should be noted that the applicability of the formulae used to calculate flexural "strength" is dubious because the development of damage in a specimen (particularly matrix cracks on the tensile side) destroys the uniformity of the specimen "beam", rendering invalid the beam theory upon which the calculations are based. However, it is generally accepted that before the onset of matrix cracking (and therefore before deviation from linearity of the force/displacement curve) the beam may be considered to be intact and that standard beam-bending equations apply. Flexural modulus measurements may therefore be considered to be comparable with tensile moduli.

Integration of force/displacement curves yields the energy consumed during tests. Whilst these data cannot be related in a straightforward way to microstructural damage processes, the method is nevertheless useful for comparative studies and general characterizations as long as one remains aware of its limitations and accompanies numerical results with a microstructural evaluation of damage.

The elastic modulus values for the HC series composites lay in the ranges 10–13 GPa for the mechanically derived values and 16–19 GPa for dynamic moduli. The XQ series moduli were in the ranges 13–17 and 19–24 GPa for the mechanical and dynamic moduli, respectively. Possible reasons for the consistently higher dynamic values are outlined later. The non-uniformity of the samples described earlier discourages the use of the mechanical property results for any detailed analysis.

If one attempts to apply a simple rule-of-mixtures relationship to the mechanical modulus results, ignoring the contribution from the matrix, expected modulus values of about 28 GPa are predicted ($= V_f E_f = 0.12 \times 230$ GPa). This expected value is higher than all of the measured values, possibly indicating that fibre degradation is occurring. Determination of a value of matrix modulus, E_m, suitable for use in calculations, is clearly problematic. The complexity of the porosity patterns seen in these materials suggests that the "normal" methods for dealing with porosity (e.g. exponential correction factors), would probably be insufficient. This is an area worthy of detailed examination.

In the HC samples, peak strengths remained approximately constant at a value of $\sim$ 130 MPa. Peak

strengths in the XQ composites decreased from 190 MPa to 90 MPa as sintering temperature was increased. An approximate rule-of-mixtures prediction of strength, again a lower bound estimate which ignores the matrix contributions, is around 420 MPa ($= V_f \sigma_f = 0.12 \times 3.5$ GPa). It is widely accepted that there is a poor correlation between flexural and tensile data. This may be attributed, in part, to the different damage mechanisms which act during flexural and tensile testing and also to the different stressed volumes in flexural and tensile specimens. Even though the highest span to depth ratios possible were employed during mechanical testing, delaminations and coinciding load drops, indicative of shear failure, were clearly observed. The standard beam-bending equations used to calculate strengths were not, therefore, strictly applicable, and this introduces another source of error into the measured strength results. This problem is not unique to this study, however. Marshall and Evans [19] reported that unidirectional SiC/LAS glass-ceramic composites tested in bending failed in compression or shear, but not in tension.

It is also highly likely that degradation of the carbon fibres during processing contributes to the difference between predicted and measured strengths. Tensile testing of both as-received and desized T300 fibre bundles has shown that a drop in fibre strength of about 35% occurs as fibres as passed through the desizing furnace [14]. This reduces the rule-of-mixtures prediction to ~ 275 MPa. Further degradation of the reinforcing fibres may be occurring during sintering.

4.2.1. Comparison of mechanical and dynamic modulus measurements

Dynamic moduli were consistently higher than those obtained mechanically. Two features may be mentioned. Firstly, the application of beam-bending equations from which the mechanical moduli were obtained is questionable. Secondly, the porosity in the materials could cause reflections of the ultrasonic pulses and hence disrupt the times of flight and calculated dynamic moduli. It should be noted that minimum times of flight were recorded for each sample. These presumably correspond to the least disturbed paths through the samples, that is to say the densest layers. Flexural testing involves subjecting only an outermost layer of the sample to tensile loads; as has already been shown, these layers inevitably contained a high degree of porosity, porosity which was frequently highly directional. Thus, it could be argued that dynamic modulus measurements were derived from denser regions of the samples than the mechanical modulus measurements. Furthermore, the ratio $E_{dyn}:E_{mech}$ decreases as sintering temperature is increased, particularly above 900 °C. This accords with the observations that the specimens sintered at 1100 and 1400 °C seem to have better densified strata than the specimens sintered at lower temperatures.

4.2.2. Toughness and fracture behaviour

Despite the difficulties associated with toughness determination for ceramic-matrix composites, the experimental data demonstrate in a consistent, if qualitative, manner that a change from a tough to a more brittle mode of fracture is seen as the sintering temperature is increased. This transition from tough to brittle behaviour may be estimated from the mechanical test and microscopy results to occur at approximately 900 °C for both the HC and XQ composites. Because matrix composition had no discernible effect on damage behaviour, discussion will now be restricted to the effect of sintering temperature on mechanical properties and damage behaviour.

As sintering temperature is increased beyond 900 °C, the toughness (work of fracture) falls rapidly, force/displacement curves show little or no post-peak load bearing, and primary crack growth occurs with minimal delamination, fibre-bridging and fibre pull-out. In the brittle region, fibre pull-out lengths were very small, typically ~ 25 μm compared to $\sim$ several 100 μm seen for samples sintered at lower temperatures. SEM studies suggested that fibre–matrix bond strength increased as sintering temperature was increased (e.g. see Fig. 18). Further, mechanical clamping of fibres by the matrix as a consequence of thermal expansion mismatches associated with α-cristobalite formation (particularly in the XQ composites) is possible. These would go some way to explaining the decrease in toughness as sintering temperature is increased. Fibre degradation would also have the effect of reducing fibre pull-out lengths.

Although the failure mechanisms of these materials have not yet been examined in any depth, evidence so far suggests that behaviour under flexure is broadly similar to that reported in the literature for other unidirectional ceramic-matrix composites, e.g. SiC/LAS [19]. Considering the samples sintered at 600–900 °C, the tensile half of the flexural specimen sees the generation of matrix cracks which run to the central plane of the sample. In this central plane shear stresses are at their maximum, encouraging delamination. These delaminations are reflected on force/displacement traces are sudden drops in load, generally followed by reloading with a lower modulus. A degree of compressive damage could be occurring at the opposite end of the beam, although this was not considered during this study. These features are all shown diagrammatically in Fig. 19. Damage behaviour frequently appeared to be strongly influenced by porosity patterns: columnar porosity seemed to provide preferred routes for tensile cracks into the centres of samples, and delaminations frequently occurred at the plane between the dense strata and the central layer of fine, dendritic porosity. The influence of porosity on cracking patterns and overall mechanical properties has not been quantified, and clearly this needs to be addressed in future work.

5. Conclusion

This work successfully demonstrates the applicability of the freeze gelation process to the fabrication of ceramic-matrix composites. Microscopy and microanalysis tools have been used to explain the influence of sintering temperature, a primary processing

parameter, on composite microstructures. These results go some way to rationalizing measured mechanical properties and observed damage mechanisms. Moreover, they permit the optimization of sintering temperature, around 900 °C for the materials studied.

The complex porosity patterns were artefacts of the freeze gelation process and must inevitably influence damage modes and engineering property values. Future work will therefore include a more rigorous examination of the development of damage in these materials and will consider the applicability of mechanical property models developed for other ceramic matrix composites.

6. Dr Richard Russell-Floyd

Sadly, Rick Russell-Floyd died during the preparation of this paper.

References

1. A. KELLY and N. H. MACMILLAN, "Strong Solids", 3rd Edn (Clarendon Press, Oxford, 1986).
2. M. RÜHLE and A. G. EVANS, *Progr. Mater. Sci.* **33** (1989) 85.
3. S. M. WIEDERHORN, *Ann. Rev. Mater. Sci.* **14** (1984) 373.
4. K. T. FABER, *Ceram. Eng. Sci. Proc.* **5** (1984) 408.
5. R. A. SAMBELL, A. BRIGGS, D. C. PHILLIPS and D. H. BOWEN, *J. Mater. Sci.* **7** (1972) 676.
6. J. A. CORNIE, Y. M. CHIANG, D. R. UHLMANN and A. MORTENSEN, *Ceram. Bull. (Am. Ceram. Soc.)* **65** (1986) 293.
7. J. R. STRIFE, J. J. BRENNAN and K. M. PREWO, *Ceram. Eng. Sci. Proc.* **11** (1990) 871.
8. F. F. LANGE, D. C. LAM, O. SUDRE and B. D. FLINN, *Mater. Sci. Eng.* **A144** (1991) 143.
9. D. C. PHILLIPS, *Compos. Sci. Technol.* **40** (1991) 17.
10. Ph. COLOMBAN, *Ceram. Int.* **15** (1989) 23.
11. R. S. RUSSELL-FLOYD, B. HARRIS, R. G. COOKE, J. LAURIE, F. W. HAMMETT, R. W. JONES and T. W. WANG, *J. Am. Ceram. Soc.* **76** (1993) 2635.
12. P. T. CURTIS, "CRAG Test methods for the measurement of engineering properties of fibre reinforced plastics", RAE-TR84102 (1984).
13. Z. STRNAD, "Glass-Ceramic Materials" (Elsevier, Oxford, 1986).
14. J. M. CHANT, unpublished work, University of Bath (1993).
15. C. CLARK-MONKS and J. M. PARKER, "Stones and Cords in Glass" (Society of Glass Technology, Sheffield, 1980).
16. D. C. PHILLIPS, R. A. SAMBELL and D. H. BOWEN, *J. Mater. Sci.* **7** (1972) 1454.
17. J. AVESTON, G. A. COOPER and A. KELLY, in "Conference on the Properties of Fibre Composites", NPL, Teddington (IPC Press, Guildford, 1971) p. 15.
18. D. C. PHILLIPS and R. W. DAVIDGE, *Br. Ceram. Trans. J.* **85** (1986) 123.
19. D. B. MARSHALL and A. G. EVANS, *J. Am. Ceram. Soc.* **68** (1985) 225.

Received 30 June
and accepted 31 October 1994